Condensation du NH$_3$ / H$_2$O avec des concentrations massiques entre 80% et 96% étude expérimentale dans un échangeur de chaleur à plaque

Tao, Xuan; Shen, Yunwei; Wang, Bo; Infante Ferreira, C.A.

Important note
To cite this publication, please use the final published version (if applicable).
Please check the document version above.

Condensation of NH₃/H₂O with mass concentrations of 80%-96%: Experimental study in a plate heat exchanger

Condensation du NH₃ / H₂O avec des concentrations massiques entre 80% et 96%: étude expérimentale dans un échangeur de chaleur à plaque

Xuan Tao [a,b,*], Yunwei Shen [a], Bo Wang [a,*], Carlos A.Infante Ferreira [b]

[a] *Cryogenics Center, Hangzhou City University, Hangzhou, 310015, China*
[b] *Process and Energy Laboratory, Delft University of Technology, Leeghwaterstraat 39, 2628 CB, Delft, The Netherlands*

ARTICLE INFO

ABSTRACT

High concentration NH₃/H₂O is suitable for Kalina cycles used for the recovery of low grade heat. Plate heat exchangers (PHEs) are compact and reduce the charge of working fluid. This paper investigates the condensation of NH₃/H₂O with NH₃ mass concentrations of 80%-96%. The vapor and liquid concentrations are close to equilibrium state, which are different from normal absorbers. The apparent heat transfer coefficients (HTCs) and frictional pressure drop are presented, covering the mass fluxes of 32–86 $\mathrm{kg m^{-2} s^{-1}}$, the averaged vapor qualities of 0.08–0.65 and the saturated pressure of 610 to 780 kPa. Larger mass fluxes noticeably increase the apparent HTCs and frictional pressure drop. At the mass concentrations of 96%, 91% and 88%, higher vapor qualities increase the apparent HTCs for large mass fluxes. The apparent HTCs decrease slightly with vapor qualities for 80% mass concentration. The experimental results are compared with those of pure NH₃. The flow patterns of high concentration NH₃/H₂O are considered as full film flow and partial film flow, which are the same as for NH₃. The mass transfer resistance deteriorates the heat transfer especially for partial film flow, which happens at small liquid mass fluxes. The mass transfer resistance has negligible influences on frictional pressure drop.

change of the secondary fluid from heat source and heat sink.

1. Introduction

Energy issues are interconnected with environmental concerns nowadays. Low carbon solutions become increasingly attractive. The utilization of low grade heat is promising to improve the sustainability of energy systems. For example, the recovery of industry waste heat reduces carbon emissions. The utilization of solar energy and ocean thermal energy provides clean approaches. The utilization of low grade heat can be implemented making use of Organic Rankine Cycles (ORCs) or Kalina Cycles. ORCs use pure refrigerants as the working fluids and have isothermal evaporation and condensation processes. The non-uniform temperature difference between the working fluids and secondary fluids brings about large thermal irreversibilities. Kalina Cycles use NH₃/H₂O mixtures. During evaporation and condensation, the temperature glide of NH₃/H₂O is utilized to match the temperature

1.1. Background

Kalina Cycles are considered to be advantagous over ORCs for medium-low temperature heat sources (Zhang et al., 2012; Wang et al., 2013). The application includes geothermal industry, cement industry, LNG cold energy recovery and ocean thermal energy conversion (Zhang et al., 2012; Atienza-Márquez et al., 2019). The advantage of Kalina Cycles is partly offset by the hindered heat transfer process because of mass transfer resistance, which increases the area of condensers and evaporators. In the plants, condensers can account for more than half of the total heat transfer area and one third of the total equipment costs (Liu et al., 2015; Heberle and Brüggemann, 2015). Plate heat exchangers (PHEs) have superior heat transfer performance and are suitable to be used as condensers (Tao and Infante Ferreira, 2019; Luo et al., 2023;

Nomenclature

Symbols

A	Actual heat transfer area [m^2]
A_f	Flow passage area [m^2]
c_p	Specific heat capacity [$Jkg^{-1}K^{-1}$]
d_g	Channel gap [mm]
d_h	Hydraulic diameter [mm]
d_p	Plate thickness [mm]
g	Gravitational constant [ms^{-2}]
G	Mass flux [$kgm^{-2}s^{-1}$]
h	Enthalpy [Jkg^{-1}]
L_p	Port-to-port plate length [mm]
$\dot{m}$	Mass flow rate [kgs^{-1}]
MC	Mass concentration of NH_3 [-]
Nu	Nusselt number [-]
P	Pressure [kPa]
Pr	Prandtl number [-]
$\dot{Q}$	Heat flow rate [W]
$\dot{q}$	Heat flux [Wm^{-2}]
Re	Reynolds number [-]
T	Temperature [°C]
U	Overall heat transfer coefficient [$Wm^{-2}K^{-1}$]
v	Specific volume [m^3kg^{-1}]
W_p	In gasket plate width [mm]
x	Vapor quality [-]

Greek symbols

α	Heat transfer coefficient [$Wm^{-2}K^{-1}$]
β	Chevron angle to flow direction [°]
Δ	Difference

δ	Uncertainty
Φ	Surface enlargement factor [-]
λ	Thermal conductivity [$Wm^{-1}K^{-1}$]
Λ_{wave}	Corrugation wavelength [mm]
μ	Dynamic viscosity [Pas]
ρ	Density [kgm^{-3}]
σ	Surface tension [Nm^{-1}]

Subscripts

after	After cooler
av	Averaged
aw	Ammonia/ water
bubble	Bubble point
de	Deceleration
dew	Dew point
ele	Elevation
eq	Equilibrium
exp	Measured value
fri	Frictional pressure drop
G	Gas or vapor
in	Inlet of test section
L	Liquid
LG	Latent liquid to vapor
mix	Mixing process
out	Outlet of test section
port	Ports of test section
sat	At saturated conditions
test	Test section
tube	Connected tube
w	Water
wall	Plate wall

Chen et al., 2019; Buscher, 2021). The combination of NH_3/H_2O and PHEs transfers large heat loads with compact structures and reduced charge of working fluids.

The bulk concentration is key for the design of Kalina Cycles operating with NH_3/H_2O. The temperature glide is required to match the temperature change of the secondary fluids from heat source and heat sink. According to thermodynamic analysis, the cycle thermal efficiency has the maximum value where the condensation temperature glide is about the same as the cooling water temperature increase (Liu et al., 2014). Fig. 1 shows the temperature glide of NH_3/H_2O, with fluid properties calculated using Refprop 10.0 (Lemmon et al., 2018). When the concentration is close to 100% and the fluid becomes almost pure NH_3, the temperature glide of NH_3/H_2O is so small that the advantage of Kalina Cycles cannot be fully exploited. When the concentration is too low, the temperature of NH_3/H_2O changes more than the secondary fluid. Moreover, lower concentration brings about larger mass transfer resistance. Larger temperature glide tends to cause greater heat transfer degradation (Shao and Granryd, 1998; Macdonald and Garimella, 2016). Thus an optimum concentration exists and is located in the high mass concentration range.

As shown in Figure 1(a), the temperature glide between bubble point and dew point is large, while the temperature glide between bubble point and the point of 0.5 vapor quality is relatively small. The available range is in low and intermediate vapor qualities of high mass concentration. In real operating conditions of Kalina Cycles, the condensation process starts from two phase and ends up with subcooling. Thus the temperature change of NH_3/H_2O is a function of the inlet vapor quality. The optimum concentration is determined by the heat capacity of the secondary fluid and the inlet vapor quality of the condenser. Apart from the temperature match, the optimum concentration also depends on the heat transfer performance of the mixture. In the actual Kalina power

plant in operation, the bulk mass concentration is higher than 80% (DiPippo, 2004; Mergner and Schaber, 2018). Moreover, NH_3/H_2O is required to have linear behavior to match the secondary fluids. According to Figure 1(b), the vapor quality range used in Kalina cycles is limited below 0. 4 for MC =0.80 and below 0.7 for MC = 0.96.

1.2. Prior work

The condensation of NH_3/H_2O is characterized by a large temperature glide. The zeotropic mixture condensation has been widely investigated using experimental and numerical methods, which are too many to be wholly listed in this Section. Instead, some representative experimental work is summarized. Fronk and Garimella (2013) reviewed the researches in tubes. In recent years, the experimental work is mostly focused on mini-channels and low ozone depletion potential (ODP) fluids, which are used for refrigerant replacement or natural gas liquification.

Table 1 summarizes the studies. Fronk and Garimella (2016a) measured the condensation of NH_3/H_2O in tubes. The apparent heat transfer coefficients (HTCs) of 90% mass concentration NH_3/H_2O show different trends compared with the HTCs of pure NH_3. Heat transfer degradation happens in high vapor quality ranges. A predictive method of NH_3/H_2O condensation is proposed based on a non-equilibrium model (Fronk and Garimella, 2016b). Zhuang et al. (2018) studied the condensation of methane/ethane and compared the experimental results with data for pure methane and ethane. The mixture HTCs can be larger than the ethane HTCs and smaller than the methane HTCs. The mixture HTCs decrease with vapor qualities for high vapor quality at the methane mass concentration of 55%. Yu et al. (2018, 2019) investigated the condensation of methane/propane with mass concentration of 41%. The mixture HTCs stay almost constant at high vapor qualities. The
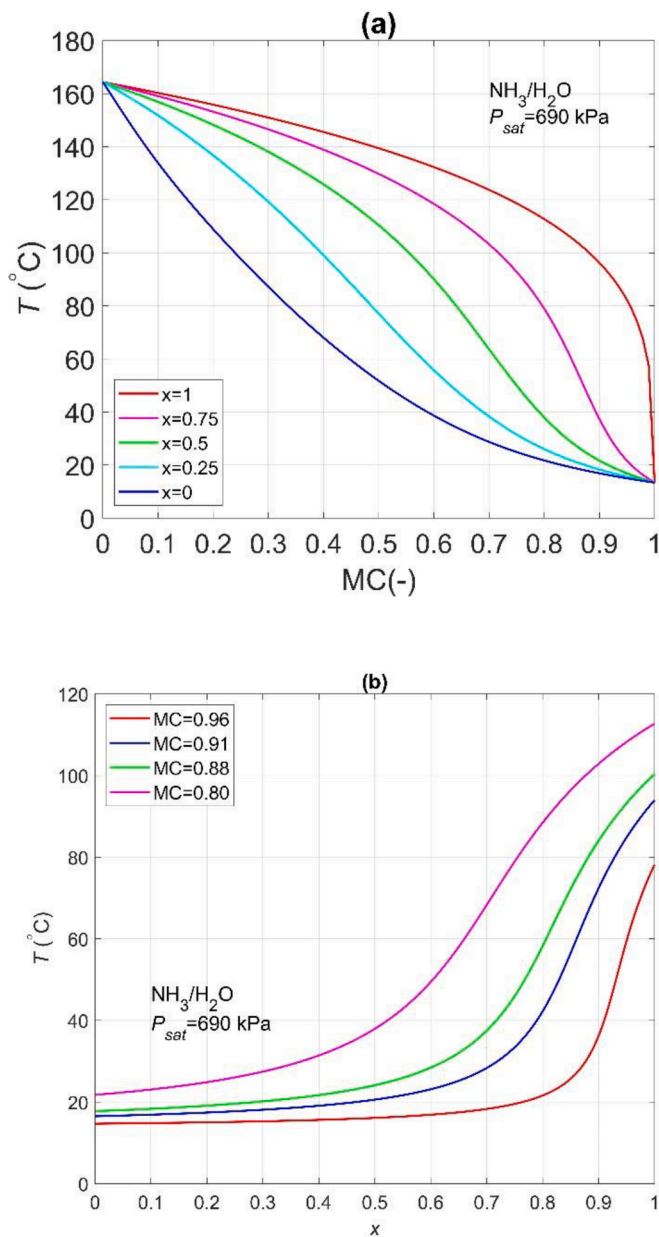
Fig. 1. (a) Temperature glide of NH_3/H_2O with varying mass concentrations. The equilibrium temperatures of bubble point, dew point and three vapor qualities are indicated. (b) Equilibrium temperature as a function of vapor quality for different mass concentrations.

condensation of zeotropic mixture has also been investigated in PHEs. Hu et al. (2017) measured the condensation of methanol/water. The 1% and 2% methanol/water have larger HTCs than pure water because of Marangoni effect. Dropwise condensation is observed. When the mass concentration is further increased, the mixture HTCs are smaller than for water. Zhang et al. (2021b) investigated the condensation of R134a/R245fa. The mixture heat transfer degrades compared with pure R134a and R245fa. The degradation is larger for low bubble point temperature and small mass fluxes. The degradation changes non-monotonically with the mass concentrations. The condensation of R1234ze(E)/R1233zd(E) is also studied. The mixture HTCs are smaller than the HTCs of pure fluids (Huang et al., 2022). The mass transfer resistance is a strong function of temperature glide. For NH_3/H_2O, methane/ethane and methane/propane, the temperature glide is large and changes nonlinearly with vapor qualities, and the sensitivity of mixture HTCs to vapor qualities is not monotonic. In other researches,

the mixture HTCs increase with vapor qualities.

NH_3/H_2O has the largest temperature glide. The condensation of NH_3/H_2O is also referred to as absorption. In the condenser of Kalina cycles, NH_3/H_2O has NH_3 mass concentrations higher than 80%. The vapor and liquid are close to thermodynamic equilibrium. Thus it is different from the normal absorbers where the liquid concentration is in the range of 30%−50% and the vapor concentration is >96% (Tao et al., 2022). The absorption of low concentration NH_3/H_2O has been investigated experimentally (Triché et al., 2017; Cerezo et al., 2009; Jung et al., 2014). But the condensation of high concentration NH_3/H_2O in PHEs has been seldomly investigated, which is closely related to flow patterns (Buscher, 2019/2022). This paper presents the experimental condensation/absorption analysis of NH_3/H_2O with the averaged mass concentration of 80%−96%. These results are compared with pure NH_3 to investigate the influence of mass transfer resistance (Tao et al., 2020; Tao and Infante Ferreira, 2020).

2. Experimental setup and data reduction

Fig. 2 shows the diagram of the experimental setup, which operates as Kalina Cycle when filled with NH_3/H_2O. NH_3/H_2O is heated and is partially vaporized in an evaporator. The two-phase mixture flows into a separator. Vapor of high NH_3 concentration flows through an expansion valve with the pressure being reduced, while liquid of relatively low NH_3 concentration flows through a recuperator and an expansion valve. The vapor and liquid are controlled to be at the same pressure and mix at the inlet of the test section. NH_3/H_2O flows from the top to the bottom of the test section, and is cooled by cold water flowing upward. NH_3/H_2O is partially condensed in the test section. It is completely condensed and is further subcooled in an after cooler. NH_3/H_2O then flows through a buffer tank, a working fluid pump, the recuperator, and flows back to the evaporator.

The test section is a gasketed plate heat exchanger (GPHE). Table 2 presents the geometrical parameters. During the experiments, the GPHE consists of three plates forming two channels and only one plate is effective for heat transfer. The condensing flow is vertical downward and resembles the actual application. NH_3/H_2O flows in a single channel to avoid flow maldistribution among channels. The actual heat transfer area is 0.064 m^2. The setup is wrapped with insulation material to minimize heat leakage. Water-water experiments have been conducted to verify the heat leakage and accuracy of the experimental setup (Tao et al., 2019). The detailed descriptions of the experimental setup and test section are given in a previous paper (Tao et al., 2020).

The bulk NH_3 concentration is determined by measuring the density of the NH_3/H_2O at liquid state together with the local temperature and pressure (Tao et al., 2019). The bulk mass concentrations are 80%−96%, which are relevant to the actual operation of Kalina cycles. The saturated pressure of NH_3/H_2O is measured at the inlet and outlet of the test section, which is the total pressure of the mixture. The operation of the cycle becomes less stable at low mass concentrations. The unstable operating conditions have not been measured. Table 3 lists the sensor features including the uncertainty and measurement range (Tao et al., 2020). The propagation of measurement uncertainty is explained in Appendix B, which refers to the approach presented by NIST (Taylor and Kuyatt, 1994). The results are given in Sections 3 and 4.

The inlet and outlet conditions of the test section are determined according to the energy balance of the after cooler and test section. In Eqs.(1)-(2), $h_{aw,in}$ and $h_{aw,out}$ are the inlet and outlet NH_3/H_2O enthalpies. The vapor qualities are determined referring to Refprop 10.0 (Lemmon et al., 2018). Eq. (3) calculates the heat transfer rate, Q_{test}, using the water side. The apparent HTC of NH_3/H_2O, α_{aw}, is determined using the equilibrium temperature of NH_3/H_2O, T_{aw}. Apparent HTC identifies the deterioration of heat transfer owing to mass transfer, but the mass transfer resistance is not calculated directly. Apparent HTC is more relevant for high concentration NH_3/H_2O at low and intermediate vapor qualities (Fronk and Garimella, 2016a). Compared with

Table 1
Condensation studies for zeotropic mixture in recent years.

Study	Channel[a]	d_h [mm]	Fluids [b]	G [kgm^{-2}s^{-1}]	T_{bubble} [°C]	ΔT_{glide} [K]	Remarks
Thonon and Bontemps (2002)	PHE, VD	8.08	Butane/propane (28%, 49%)	2.1–21.4	34–62	8–13	The mixture HTCs of turbulent flow are accurately predicted using the Silver-Bell-Ghaly method, while those of laminar flow are over-predicted.
Mancin et al. (2012)	PHE, VD	–	R407C	15–40	37	5	The zeotropic mixture R407C has larger mass transfer resistance compared with azeotropic mixture R410A.
Del Col et al. (2015)& Deng et al. (2019)	Tubes, H	0.8, 0.96	R32/R1234ze(E) (23%, 25%, 46%)	100–800	23–47	8–12	The mixture HTCs are smaller than the linear interpolation of pure fluids. The mass transfer resistance of annular flow and stratified flow is analysed.
Fronk and Garimella (2016a/b)	Tubes, H	0.98, 1.44, 2.16	NH$_3$/H$_2$O (80%, 90%, >96%)	50–200	40–49	58–89	The heat transfer model is based on a non-equilibrium model.
Macdonald and Garimella (2016)	Tubes, H	7.75, 14.45	Ethane/propane (33%, 67%)	150–450	25–60	6–13	The heat transfer data are analyzed using both equilibrium model and non-equilibrium model.
Ghim and Lee (2016)	Tube, H	7.75	n-Pentane/R245fa (91.2%)	100–150	65	9	The mixture HTCs are lower than the HTCs of n-Pentane but are higher than those of R245fa.
Hu et al. (2017)& Zhou et al. (2018)	PHE, VD	5	Methanol/water (1%, 2%, 5%, 10%, 20%)	6.9	67–94	0–7	A heat transfer correlation is developed considering the Marangoni effect.
Zhuang et al. (2018)	Tube, H	4	Methane/ethane (16%, 39%, 55%)	98–257	−104 to −51	37–52	The flow patterns were observed, and a flow pattern based heat transfer correlation was developed.
Yu et al. (2018, 2019)	Tube, HC	10	Methane/propane (41%)	200–400	−66 to −94	37–47	The flow patterns were observed, and a flow pattern based heat transfer correlation was developed.
Mazumder et al. (2021)	Tube, H	4.35	R32/R1234ze(E) (25%, 45%, 75%)	100–500	35–45	3–11	A generalized heat transfer correlation is proposed considering mass transfer resistance.
Zhang et al. (2021a)	RC, H	1 [c]	R134a/R245fa (10%, 30%, 70%)	100–1000	20–40	9–15	The flow patterns were observed. A heat transfer correlation was developed based on mass concentration and temperature glide.
Zhang et al. (2021b)	PHE, VD	3.4	R134a/R245fa (22.5%, 43.1%, 64.0%, 79.5%, 92.3%)	21.0–79.6	30–50	3–14	The mixture HTCs are well predicted using the modified Silver-Bell-Ghaly method.
Huang et al. (2022)	PHE, VD	3.4	R1234ze(E)/R1233zd(E) (14.8%, 35.2%, 53.8%, 81.3%)	25–78	30–50	5–13	The mixture HTCs are well predicted using the modified Silver-Bell-Ghaly method.

[a] VD: Vertical downward; H: Horizontal; HC: Helically coiled; RC: Rectangular channel.
[b] The numbers in the bracket are the mass concentrations of the first component.
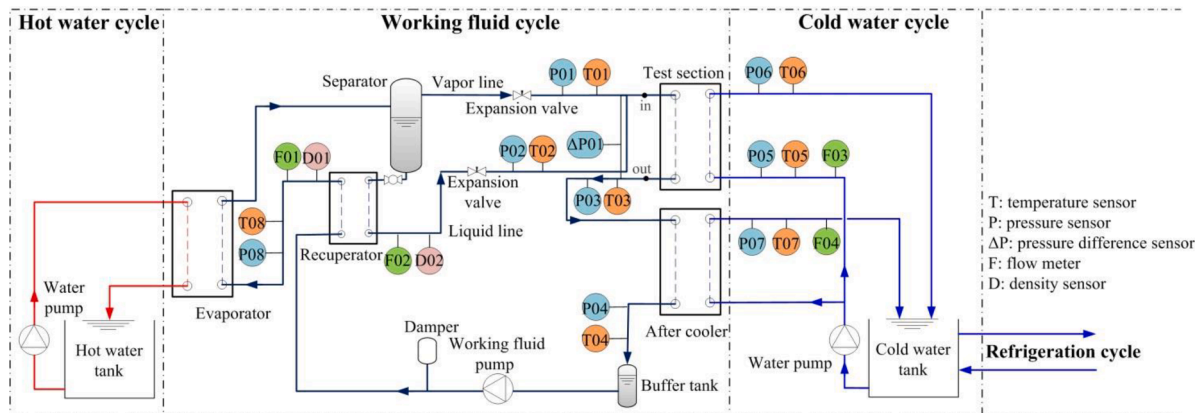[c] This is the gap of rectangular channel.

Fig. 2. Experimental setup diagram including the working fluid cycle, cold water cycle and hot water cycle.

Table 2
Geometrical parameters of the test section.

Plate number –	L_p mm	W_p mm	A m^2	d_h mm	β	ϕ –	d_g mm	d_p mm	Λ_{wave} mm
3	668	95	0.064	2.99	63°	1.15	1.72	0.58	6.67

intermediate concentrations or complete condensation, the temperature glide during partial condensation within two-phase region is relatively small. Additionally, apparent HTC is comparable with the HTC of pure NH$_3$. The water HTC, α_w, is determined using single-phase heat transfer experiments and is given in Eq. (4) (Tao et al., 2019).

$$h_{aw,out} = h_{aw,04} + \frac{\dot{Q}_{after}}{\dot{m}_{aw,01}} = h_{aw,04} + \frac{c_{p,w}\dot{m}_{w,04}\left(T_{w,07} - T_{w,05}\right)}{\dot{m}_{aw,01}} \tag{1}$$

Table 3
Specification of the sensors.

| Sensors	Type	Sensor uncertainty	Range
Temperature	PT-100	±0.05 °C	2 /50 °C
NH$_3$ pressure	Absolute	±0.05% FS	0/1000 kPa
NH$_3$ pressure	Gage	±0.5% FS	0/1000 kPa
Water pressure	Gage	±0.5% FS	0 /250 kPa
Differential pressure	SITRANS P DS	±0.3% FS	1.6 /160 kPa
NH$_3$ overall flow	Coriolis	±0.2% RD	0 /0.02 kgs^{-1}
NH$_3$ liquid flow	Coriolis	±0.2% RD	0 /0.013 kgs^{-1}
Water flow	Turbine	±7.2 Lh^{-1}	30 /3000 Lh^{-1}
NH$_3$ density	Anton Paar	±0.1 kgm^{-3}	–
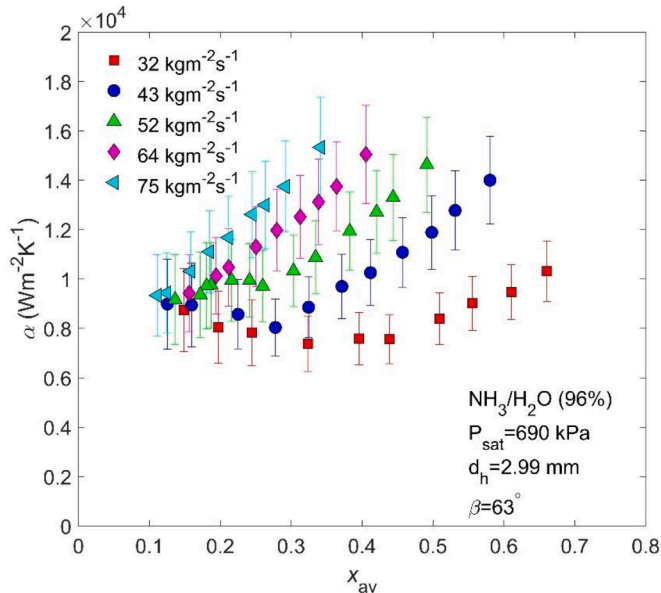
Fig. 3. Apparent HTCs with varying averaged vapor quality at different mass fluxes. The bulk mass concentration is 96%.
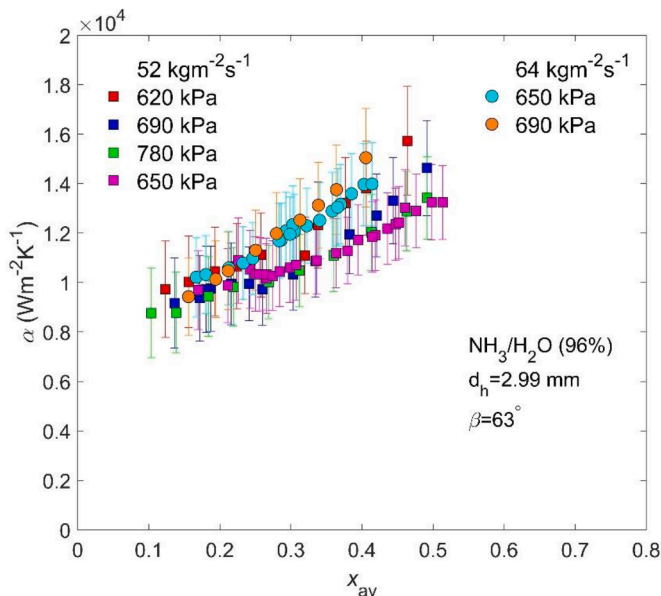

Fig. 4. Apparent HTCs with varying averaged vapor quality at different saturated pressures. The bulk mass concentration is 96%.

$$h_{aw,in} = h_{aw,out} + \frac{\dot{Q}_{test}}{\dot{m}_{aw,01}} = h_{aw,out} + \frac{c_{p,w}\dot{m}_{w,03}\left(T_{w,06} - T_{w,05}\right)}{\dot{m}_{aw,01}} \tag{2}$$

$$\dot{Q}_{test} = \dot{m}_w c_{p,w}\left(T_{w,out} - T_{w,in}\right) = \dot{m}_{aw}\left(h_{aw,i_n} - h_{aw,out}\right)$$
$$= UA \frac{\left(T_{aw,in} - T_{w,out}\right) - \left(T_{aw,out} - T_{w,in}\right)}{\ln\dfrac{T_{aw,in} - T_{w,out}}{T_{aw,out} - T_{w,in}}}$$
$$= \frac{A}{\dfrac{1}{\alpha_{aw}} + \dfrac{d_p}{\lambda_{wall}} + \dfrac{1}{\alpha_w}} \frac{\left(T_{aw,in} - T_{w,out}\right) - \left(T_{aw,out} - T_{w,in}\right)}{\ln\dfrac{T_{aw,in} - T_{w,out}}{T_{aw,out} - T_{w,in}}} \tag{3}$$

$$Nu_w = \frac{\alpha_w d_h}{\lambda_w} = 0.275 Re_w^{0.7} Pr_w^{1/3} \qquad 320 \leq Re_w \leq 2600 \tag{4}$$

In Eq. (5), the frictional pressure drop, $\Delta P_{fri,aw}$, is calculated by subtracting the other components from the measured pressure drop, $\Delta P_{exp,aw}$. Eqs. (6)-(7) calculate the pressure drops of inlet and outlet ports, $\Delta P_{inport,aw}$ and $\Delta P_{outport,aw}$ Collier and Thome, 1994). In Eqs. (8)-((9), the deceleration pressure rise, $\Delta P_{de,aw}$, and elevation pressure rise, $\Delta P_{ele,aw}$, are calculated (Collier and Thome, 1994). The mixing pressure drop, $\Delta P_{mix,aw}$, specifies the spraying of liquid into vapor through orifices (Jankowski et al., 2008). More details of the data reduction are explained in Tao et al. (2019) and Tao et al. (2020).

$$\Delta P_{fri,aw} = \Delta P_{exp,aw} - \Delta P_{inport,aw} - \Delta P_{outport,aw} - \Delta P_{mix,aw} + \Delta P_{de,aw} + \Delta P_{ele,aw} \tag{5}$$

$$\Delta P_{in\,port,aw} = G_{tube}^2 v_L \frac{A_{tube}}{A_{port}}\left(1 - \frac{A_{tube}}{A_{port}}\right)\left(1 + \frac{v_G - v_L}{v_L}x\right) \tag{6}$$

$$\Delta P_{out\,port,aw} = \frac{G_{tube}^2 v_L}{2}\left(\frac{1}{0.591} - 1\right)^2\left(1 + \frac{v_G - v_L}{v_L}x\right) \tag{7}$$

$$\Delta P_{de,aw} = G^2\left(v_G - v_L\right)\left(x_{in} - x_{out}\right) \tag{8}$$

$$\Delta P_{ele,aw} = \rho_{av} g L_p \tag{9}$$

3. Apparent heat transfer coefficient

The apparent HTCs and frictional pressure drop of NH$_3$/H$_2$O are measured for the bulk mass concentrations of 80%−96%. The NH$_3$/H$_2$O has the mass fluxes of 32–86 kgm^{-2}s^{-1} and the averaged vapor qualities of 0.08–0.65, the vapor qualities suitable for Kalina cycle applications, see Figure 1(b). The corresponding superficial liquid and vapor velocities are 0.01–0.12 ms^{-1} and 1.23–6.19 ms^{-1}, respectively. The saturated pressures are 610–780 kPa, corresponding to the bubble point temperatures of 11.6–18.5 °C.

The mass fluxes of the cold water were maintained to be the maximum value allowed by the setup, so the corresponding heat transfer resistance is restricted. The water HTCs are larger than 20,000 Wm^{-2}K^{-1}. Consequently, the heat transfer resistance of the condensation side is larger than that of the water side. In actual condensers, the vapor qualities change remarkably from the inlet to the outlet because of the large heat duties. The concentrations of the vapor and liquid change significantly. The temperature glide of the mixture affects the distribution of vapor quality. During the measurements of this study, the change of the vapor qualities is smaller than 0.2, and the variations of two-phase concentrations are limited. The experimental results show quasi-local characteristics.

3.1. Mass concentration of 96%

Fig. 3 shows the sensitivity of apparent HTCs to averaged vapor qualities and mass fluxes. The NH$_3$ mass concentration is 96% ± 1%. The concentration increases slightly with vapor qualities during
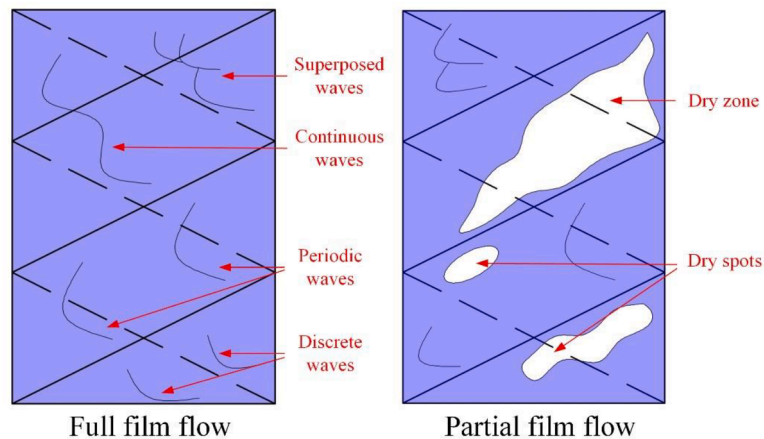
Fig. 5. Schematics of full film flow and partial film flow, adapted from Tao et al. (2020).

operation. The saturated pressure is 690 kPa, and corresponds to a bubble point of 14.7 °C. Apparent HTCs increase sharply with vapor qualities. The increase is 1.5 times when the vapor qualities rise from 0.2 to 0.4.

A comparison is made with NH_3 condensation, which is reported in the previous paper (Tao et al., 2020). As shown in the Appendix A, both NH_3/H_2O and NH_3 have large two-phase density ratio. The thickness of condensate film decreases with higher vapor quality. The apparent HTCs of NH_3/H_2O are smaller than the HTCs of pure NH_3 especially at high vapor qualities. NH_3/H_2O has a large temperature glide. The mass transfer resistance deteriorates the heat transfer distinctly even the mass concentration is as high as 96%. The mass transfer resistance is a function of the concentration difference between the vapor and liquid. NH_3 is more volatile than H_2O. H_2O condenses preferentially, while the rest NH_3 accumulates close to the vapor-side interface. The diffusion of H_2O is restricted in this zone. Consequently, concentration is different among the bulk vapor, bulk liquid and two-phase interface. Concentration gradients build mass transfer resistances and sensible heat transfer resistances. H_2O tends to condense first at high vapor qualities, where the vapor concentration changes significantly. Larger concentration gradients result in stronger mass transfer resistance. At lower vapor qualities, the vapor phase is almost pure NH_3 since most H_2O has already been condensed, so the HTCs are consistent with pure NH_3 (Fronk and Garimella, 2016a).

Larger mass fluxes always increase the apparent HTCs. When the mass flux increases from 32 to 75 $kgm^{-2}s^{-1}$, the apparent HTCs nearly doubles. Larger mass fluxes bring about higher flow velocity and thicker liquid film, which are self-compensating. Furthermore, larger mass fluxes enhance the turbulence for the flow of the mixture. Rolls and ripples mix the fluid and reduce the concentration gradients. Thus the effect of mass transfer resistance is suppressed. The trend of NH_3/H_2O is different from that of pure NH_3, whose HTCs are less sensitive to mass fluxes (Tao et al., 2020). The data in Fig. 3 have an averaged uncertainty of ±14.3%.

Fig. 4 shows the influence of saturated pressure for two mass fluxes. When the mass flux is 52 $kgm^{-2}s^{-1}$, higher saturated pressure slightly decreases apparent HTCs for 620 kPa, 690 kPa and 780 kPa. The decrease is less than 10%. The difference is larger for high vapor qualities. Similar to pure NH_3, higher saturated pressure increases the vapor density and reduces the flow velocity (Tao et al., 2020). Smaller shear force weakens heat transfer. Additionally, during the condensation of NH_3/H_2O, the sensible heat of vapor is transferred through the two-phase interface. Higher saturated pressure reduces the vapor-phase HTCs and hinders the overall heat transfer. The apparent HTCs of 650 kPa have lower values. The possible reason is that the mass flux fluctuation induced by the membrane pump is not fully eliminated by the pulsation damper during the 650 kPa experiments. For the mass flux of

64 $kgm^{-2}s^{-1}$, the apparent HTCs of 690 kPa are similar to those of 650 kPa since the difference of the saturated pressure is small. Generally, the influence of saturated pressure is relatively small compared with the effects of mass flux and vapor quality. In Fig. 4, the averaged uncertainty of apparent HTCs is ±14.1%.

According to previous visualization experiments of NH_3 condensation in PHEs, the flow patterns are full film flow at large liquid mass fluxes and partial film flow at small liquid mass fluxes (Tao et al., 2020). The schematics are shown in Fig. 5. During full film flow, the wall surface of the PHE is completely wetted by the liquid film. The strong shear force at the two-phase interface brings about waves. For partial film flow, parts of the wall are dry. Flow patterns are a function of two-phase fluid properties, operating conditions and channel geometries. The flow patterns for NH_3/H_2O are considered to be the same as for NH_3. As shown in the Appendix A, the fluid properties change continuously with concentration. The density, viscosity and surface tension of high concentration NH_3/H_2O approach those of pure NH_3. The NH_3/H_2O experiments had the same operating ranges of mass fluxes and vapor qualities as for the NH_3 experiments. Additionally, the same test section was used. Both full film flow and partial film flow are separated flow. The influences of liquid and vapor mass fluxes are investigated separately.

Figure 6(a) presents the apparent HTCs of NH_3/H_2O with varying liquid and vapor mass fluxes, whose averaged bulk mass concentration is 96%. The saturated pressure is 690 kPa. The ratio of vapor mass flux to liquid mass flux is in the range of 0.17–1.78. The liquid mass concentration is above 90% at the inlet and above 94% at the outlet. The vapor mass concentration is higher than 99%. The HTCs of NH_3 are shown for comparison in Figure 6(b), which have been published in a previous paper (Tao et al., 2020). In Figure 6(a), the apparent HTCs increase with larger liquid mass fluxes at small values, and stay almost constant at larger values. The change of the slopes indicates the transition of flow patterns. The value of liquid mass flux for this change is similar to that for NH_3 shown in Fig. 6(b), which is 30–40 $kgm^{-2}s^{-1}$. The flow patterns for high concentration NH_3/H_2O are expected to be the same as for NH_3 (Tao et al., 2020).

According to Tao et al. (2020), partial film flow happens at small liquid mass fluxes. As shown in Fig. 5, the wall is composed of wetted zones and dry zones. In the wetted zones, the vapor contacts the two-phase interface and is absorbed by the liquid. Heat and mass are transported through the liquid film. In the dry zones, the vapor is in contact with the wall directly. The phase change takes place since the wall temperature is lower than the bubble point of NH_3/H_2O. The local HTC at the wall is lower than that at the two-phase interface where the two-phase concentration difference drives the mass transfer. The area of the wetted zones increases with liquid mass fluxes, promoting the overall heat transfer. Full film flow applies at a certain liquid mass flux
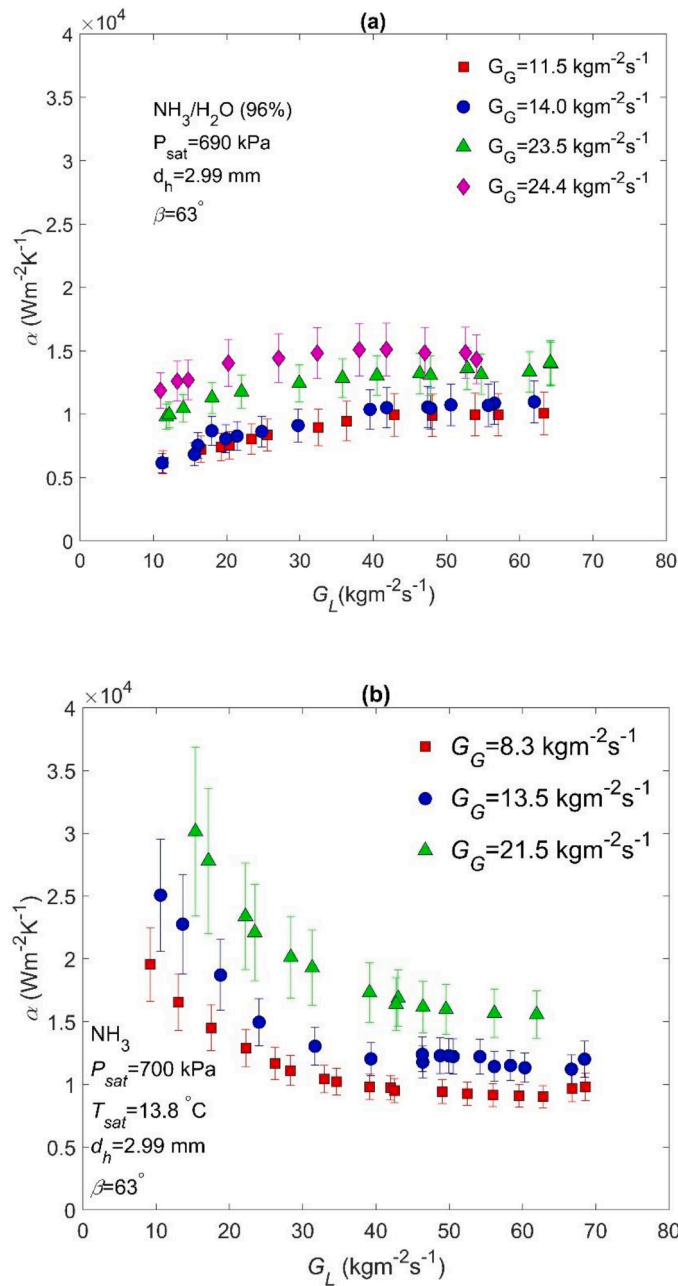
Fig. 6. HTCs with varying liquid and vapor mass fluxes: (a) apparent HTCs of 96% NH_3/H_2O, (b) HTCs of NH_3 (Tao et al., 2020).
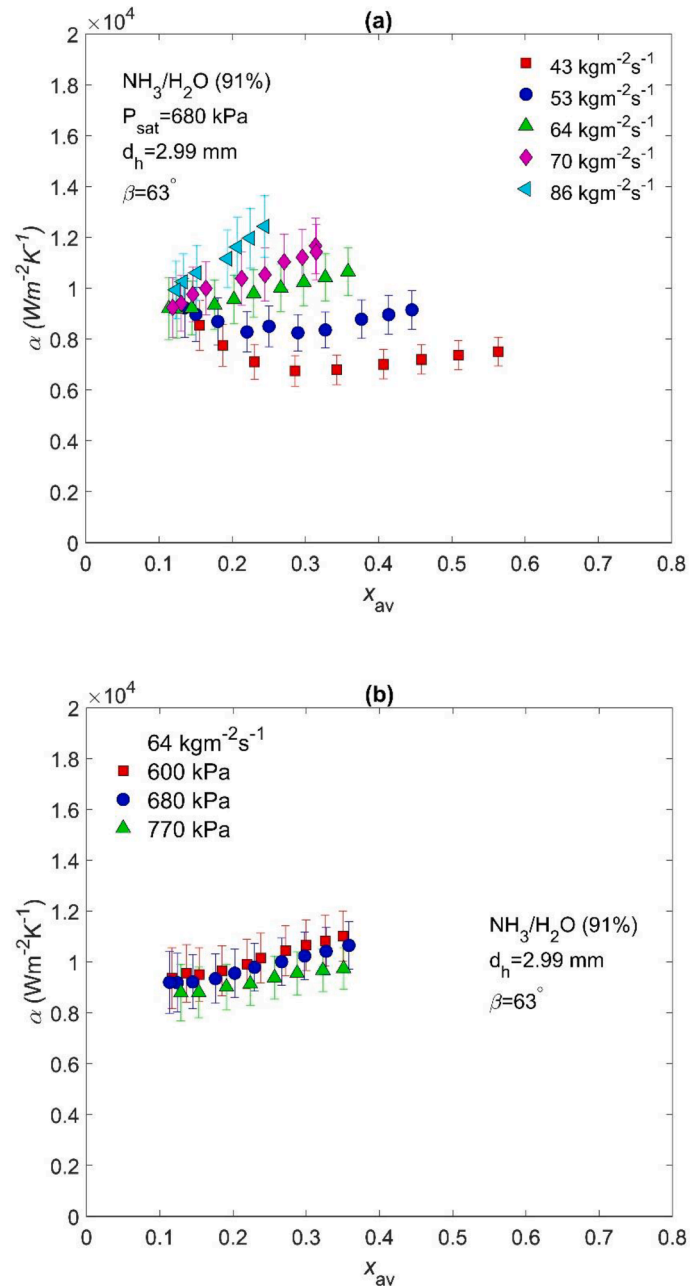

Fig. 7. Apparent HTCs with varying averaged vapor quality at (a) different mass fluxes and (b) different saturated pressures. The bulk mass concentration is 91%.

when the wall gets wetted completely. All the heat is transferred through the two-phase interface. The apparent HTCs become almost constant. The slope of HTCs is different from that of NH_3 in Figure 6(b). Mixture condensation happens at the dry zones of partial film flow. The vapor concentration is higher than 99%. According to the experimental results, even minor H_2O brings about noticeable mass transfer resistance and deteriorates the phase change heat transfer at the wall surface. Consequently, the apparent HTCs of NH_3/H_2O are significantly smaller than the HTCs of NH_3. The ratio can reach four times. For full film flow and the wetted zones of partial film flow, the mass transfer resistance hinders the heat transfer. Nevertheless, the concentration difference of NH_3 promotes the absorption of NH_3 vapor into the liquid, which simultaneously drives the heat transfer. These two effects counteract each other. Thus the apparent HTCs of NH_3/H_2O are slightly smaller than the HTCs of NH_3.

Larger two-phase mass fluxes increase the flow velocities and

enhance the shear force at liquid-vapor interface, which promotes heat transfer. In Figure 6(a), larger vapor mass fluxes significantly increase the apparent HTCs. NH_3/H_2O has a large two-phase density ratio. The vapor mass flux contributes noticeably to the flow velocity. However, the influence of liquid mass flux is self-compensating. Apart from enhanced shear force, larger liquid mass fluxes thicken the liquid film, which acts as heat transfer resistance. Consequently, for full film flow, the apparent HTCs stay almost constant with increasing liquid mass fluxes.

3.2. Mass concentration of 91%

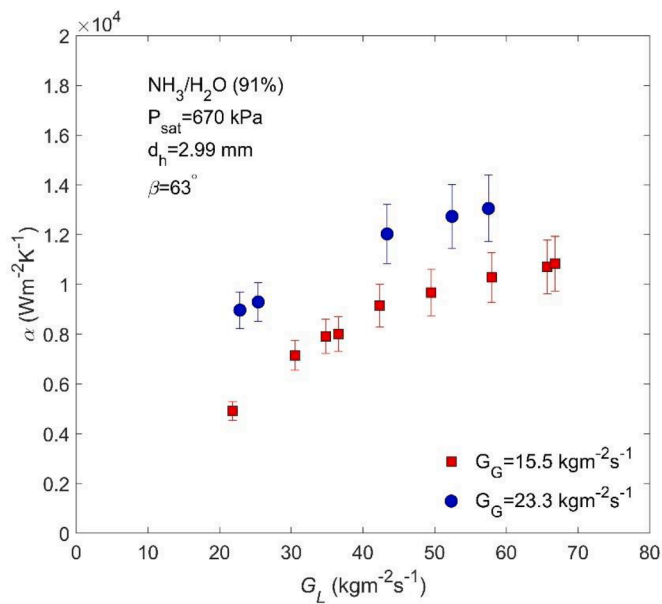Fig. 7 shows the apparent HTCs for different averaged vapor

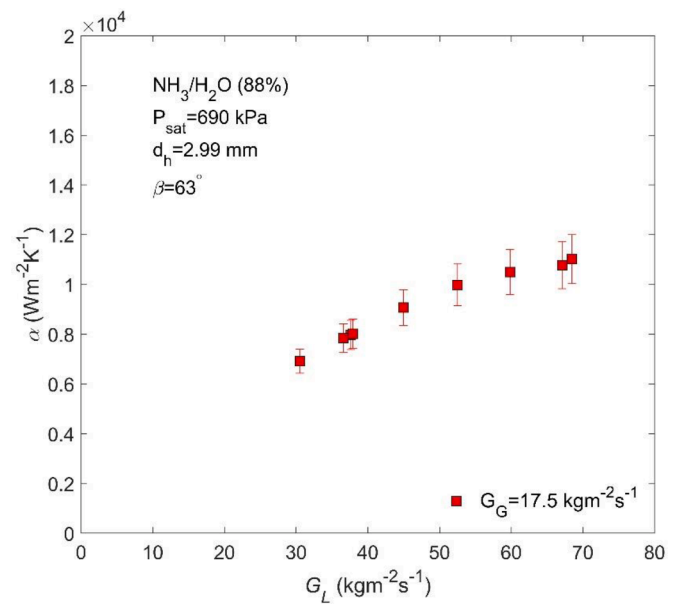**Fig. 8.** Apparent HTCs with varying liquid and vapor mass fluxes. The bulk mass concentration is 91%.

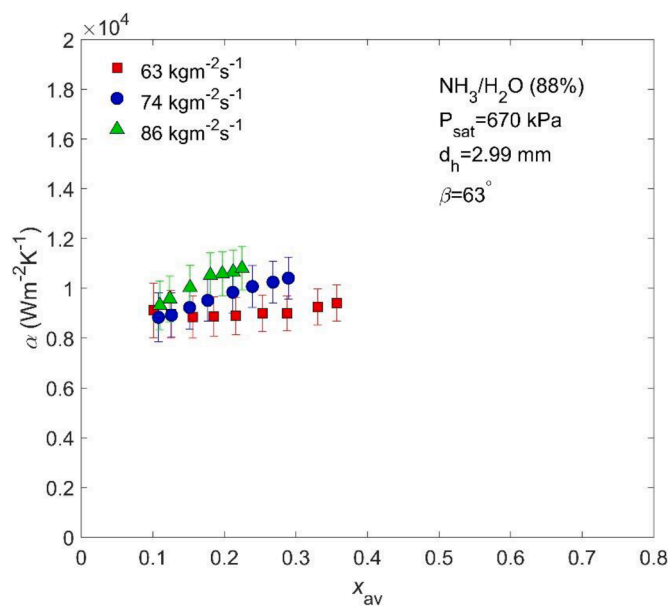**Fig. 10.** Apparent HTCs with varying liquid mass fluxes. The bulk mass concentration is 88%.

Fig. 9. Apparent HTCs with varying averaged vapor quality at different mass fluxes. The bulk mass concentration is 88%.
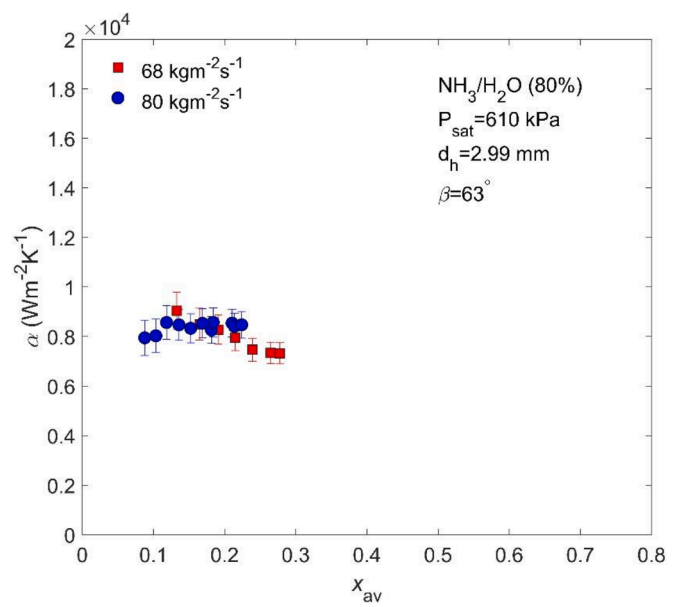

Fig. 11. Apparent HTCs with varying averaged vapor quality at different mass fluxes. The bulk mass concentration is 80%.

qualities, mass fluxes and saturated pressures. The NH_3 mass concentration is 91%. According to Figure 7(a), for the mass fluxes of 43 and 53 $kgm^{-2}s^{-1}$, the apparent HTCs decrease slightly with vapor qualities at small values but increase marginally with vapor qualities at large values. The mass transfer resistance has a large effect at small mass fluxes. When the mass fluxes are larger than 64 $kgm^{-2}s^{-1}$, the apparent HTCs increase with vapor qualities. Larger mass fluxes raise the apparent HTCs by intensifying the mixing of the flow, which reduces the effect of mass transfer resistance. At the largest mass flux, the apparent HTCs increase from 10,000 to 12,400 $Wm^{-2}K^{-1}$. The trend is similar to that of the 96% mass concentration. In Figure 7(b), the apparent HTCs decrease slightly with higher saturated pressure, which agrees with Fig. 4 and shows the influence of saturated pressure.

Fig. 8 shows the apparent HTCs with varying liquid and vapor mass fluxes for the bulk mass concentration of 91%. The apparent HTCs

increase noticeably with larger liquid mass fluxes at small values, and increase moderately at larger values. The transition is gradual and happens at 40–50 $kgm^{-2}s^{-1}$, which reflects the transition from partial film flow to full film flow. In Fig. 6 of pure NH_3 and 96% NH_3/H_2O, the data points have a flat trend at large liquid mass fluxes, which is different from Fig. 8. The apparent HTCs of 91% NH_3/H_2O are smaller than those of 96% NH_3/H_2O. Lower NH_3 concentration increases the mass transfer resistance. The liquid mass flux plays an important role to overcome the mass transfer resistance. The influence of larger shear force dominates over thicker liquid film. Thus the apparent HTCs keep increasing. As presented in the Appendix A, lower NH_3 concentration increases the liquid density and surface tension of NH_3/H_2O. Larger surface tension hinders the wetting characteristics (Hart et al., 1989; Tao and Infante Ferreira, 2020). The flow pattern of 91% NH_3/H_2O changes at larger liquid mass flux than it changes for pure NH_3.
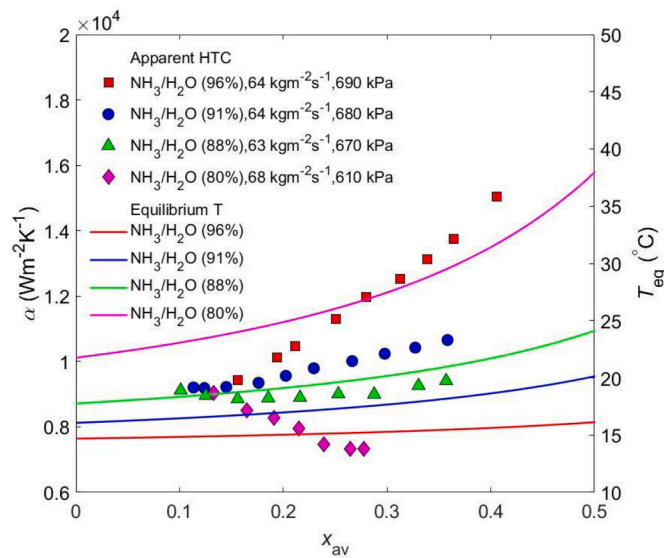
Fig. 12. Comparison of apparent HTCs and equilibrium temperature for different mass concentrations. .

Fig. 14. Frictional pressure drop with varying averaged vapor quality at different condensation pressures. The bulk mass concentration is 96%.

discussed in Section 3.1, H_2O condenses preferentially at high vapor qualities. The diffusion of H_2O hinders the heat transfer. The two-phase interface temperature is lower than the equilibrium temperature, which reduces the temperature driving force.

3.4. Impact of mass concentration

In Fig. 12, the apparent HTCs of different mass concentrations are compared, and the mass fluxes are kept almost constant. The apparent HTCs decrease with lower mass concentrations especially for high vapor qualities. The equilibrium temperature of NH_3/H_2O is also shown, and the temperature glide between bubble point and the point of 0.3 vapor quality can be referred to. When the mass concentration decreases from 96% to 80%, this temperature glide increases from 0.6 to 5.7 K. The change of equilibrium temperature is sharper at high vapor qualities. The mass transfer resistance has more noticeable effects in the range of low mass concentrations and high vapor qualities. In Figs. 3-11, the maximum vapor qualities are limited by the heating capacity and heating temperature of the setup. Please notice that the experimental data significantly covers the range of vapor qualities relevant for Kalina cycle applications, see Figure 1(b).

4. Frictional pressure drop

4.1. Mass concentration of 96%

Fig. 13 shows the frictional pressure drop of NH_3/H_2O as a function of averaged vapor qualities and mass fluxes. Vapor qualities have a significant influence on the frictional pressure drop. In the vapor quality range of 0.1 to 0.35, the frictional pressure drop triples. It is attributed to the large two-phase density ratio of NH_3/H_2O. The flow of NH_3/H_2O is separated flow. The two-phase pressure drop is composed of vapor pressure drop, liquid pressure drop and interface pressure drop. Vapor pressure drop is dominant. Higher vapor quality increases the volume flux and shear force. Larger mass fluxes sharply increase the frictional pressure drop and intensify the influence of vapor qualities. When the mass fluxes double from 32 to 64 $kgm^{-2}s^{-1}$, the frictional pressure drop becomes more than four times larger. According to the comparison with pure NH_3, the mixture effect can be neglected for frictional pressure drop. The trend of NH_3/H_2O is the same as for NH_3 (Tao et al., 2020). The averaged uncertainty is $\pm15.8\%$. The uncertainty analysis considers
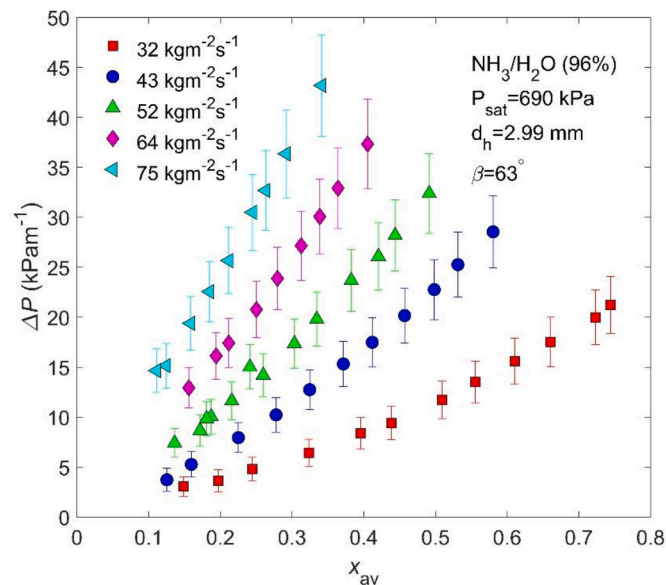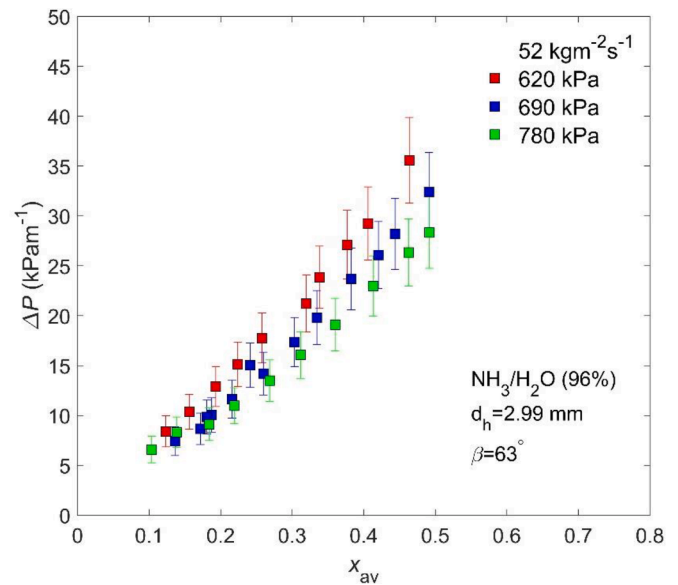

Fig. 13. Frictional pressure drop with varying averaged vapor quality at different mass fluxes. The bulk mass concentration is 96%.

3.3. Mass concentration of 88% and 80%

Fig. 9 shows the apparent HTCs for the mass concentration of 88%. The sensitivity to the averaged vapor qualities and mass fluxes are shown. When the mass flux is 63 $kgm^{-2}s^{-1}$, the apparent HTCs are almost constant. At larger mass fluxes, the apparent HTCs increase slightly with vapor qualities.

In Fig. 10, the mass concentration is also 88%. The apparent HTCs increase with liquid mass fluxes, which is similar to Fig. 8. With increasing liquid mass fluxes, a larger area of the wall is wetted by the liquid. The vapor is absorbed at the two-phase interface, and the heat transfer is enhanced.

Fig. 11 shows the apparent HTCs with the bulk mass concentration of 80%. When the mass flux is 68 $kgm^{-2}s^{-1}$, the apparent HTCs decrease slightly with vapor qualities. The apparent HTCs are almost constant at 8000 $Wm^{-2}K^{-1}$ for 80 $kgm^{-2}s^{-1}$. The trends are different from pure NH_3 and are the results of large mass transfer resistance (Tao et al., 2020). As

Fig. 15. Frictional pressure drop with varying liquid and vapor mass fluxes: (a) 96% NH$_3$/H$_2$O, (b) NH$_3$ (Tao et al., 2020).

Fig. 16. Frictional pressure drop with varying averaged vapor quality at (a) different mass fluxes and (b) different saturated pressures. The bulk mass concentration is 91%.

the sensor accuracy and flow fluctuation (Tao et al., 2020).

Fig. 14 shows the influence of saturated pressures on frictional pressure drop. The influence becomes apparent with increasing vapor qualities. The decrease is more than 20% when the saturated pressure changes from 620 to 780 kPa. Higher saturated pressure increases the vapor density and reduces the volume flux. Consequently, the momentum dissipation is decreased. The data have an averaged uncertainty of ±15.0%.

Fig. 15 shows the influence of liquid and vapor mass fluxes. For NH$_3$/H$_2$O, the frictional pressure drop increases linearly with both mass fluxes, which is the same as for NH$_3$ (Tao et al., 2020). The change of flow patterns does not affect the trend of frictional pressure drop. The sharp trend indicates separated flow. Mass transfer resistance has negligible effects on momentum transport characteristics, which further confirms that the flow patterns of high concentration NH$_3$/H$_2$O are the same as for NH$_3$.
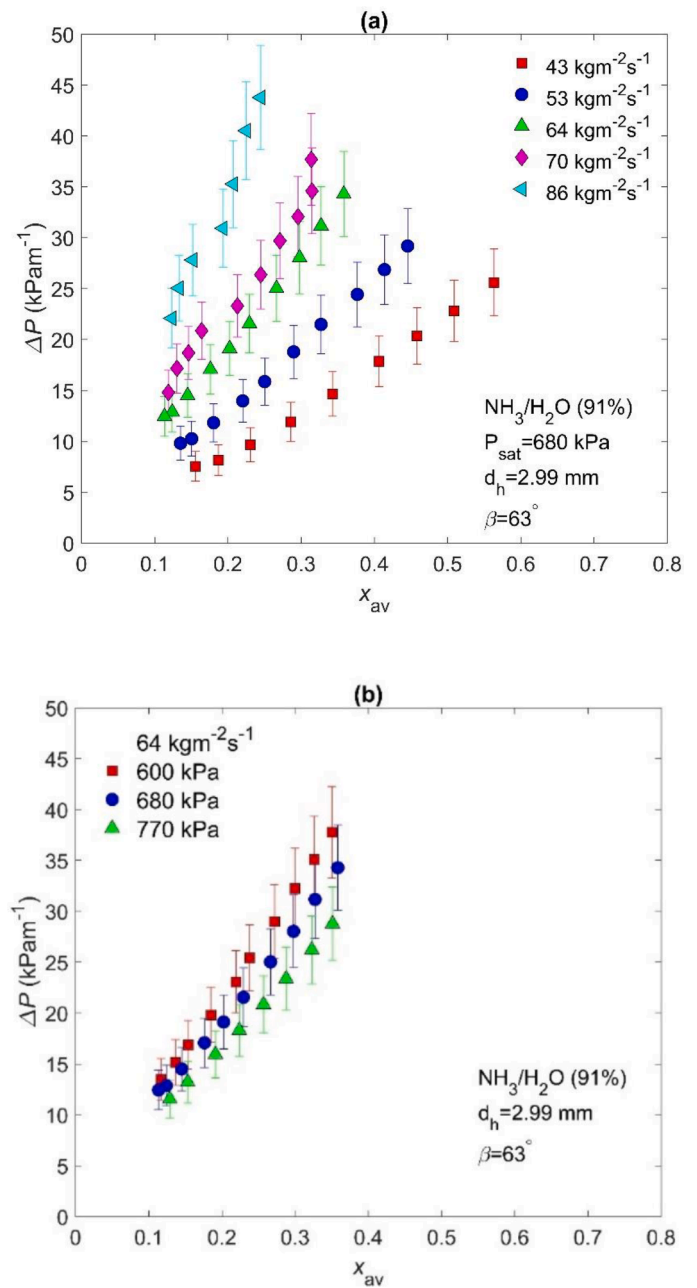
4.2. Mass concentration of 91%

Fig. 16 shows the frictional pressure drop of NH$_3$/H$_2$O with mass concentration of 91%. In Figure 16(a), the frictional pressure drop increases sharply with the averaged vapor qualities and mass fluxes. The increase rate is almost the same as that of 96% NH$_3$/H$_2$O. The increase with vapor qualities is steep at large mass fluxes. Figure 16(b) shows the influence of saturated pressures. Higher saturated pressures slightly reduce the frictional pressure drop.

Fig. 17 shows the frictional pressure drop with varying liquid and vapor mass fluxes. The frictional pressure drop increases linearly with liquid mass fluxes. When the vapor mass fluxes increase from 15.5 to 23.3 kgm^{-2}s^{-1}, the frictional pressure drop almost doubles.

Fig. 17. Frictional pressure drop with varying liquid and vapor mass fluxes. The bulk mass concentration is 91%.

Fig. 19. Frictional pressure drop with varying liquid mass fluxes. The bulk mass concentration is 88%.

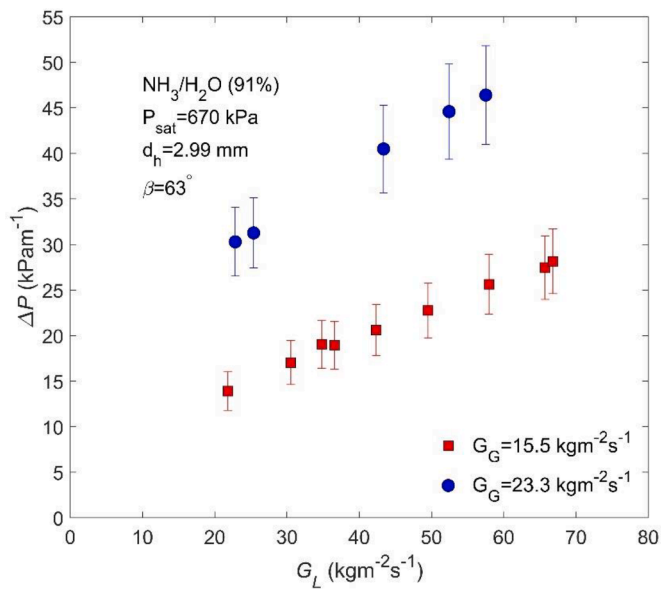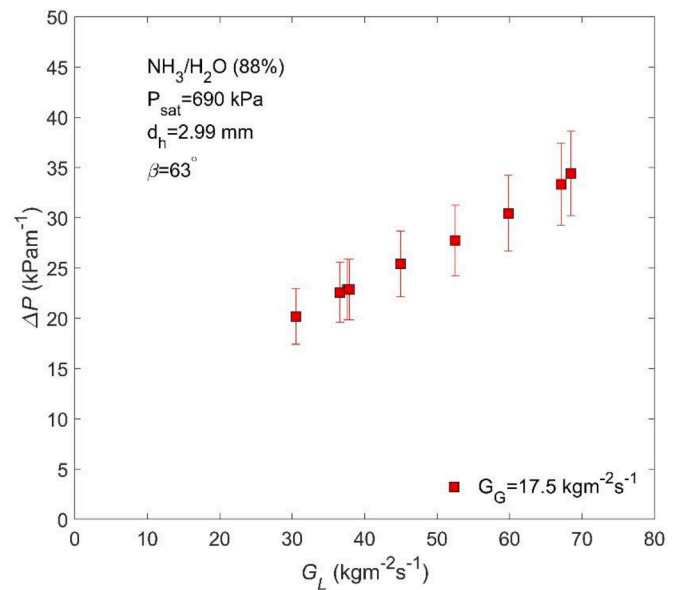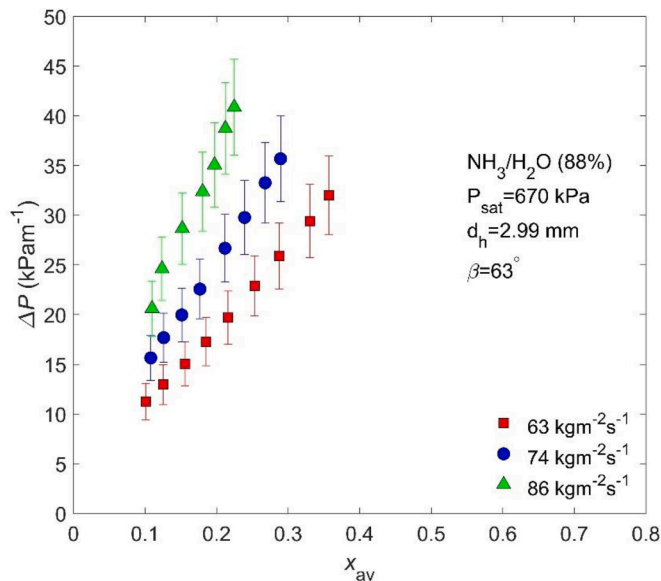**Fig. 18.** Frictional pressure drop with varying averaged vapor quality at different mass fluxes. The bulk mass concentration is 88%.
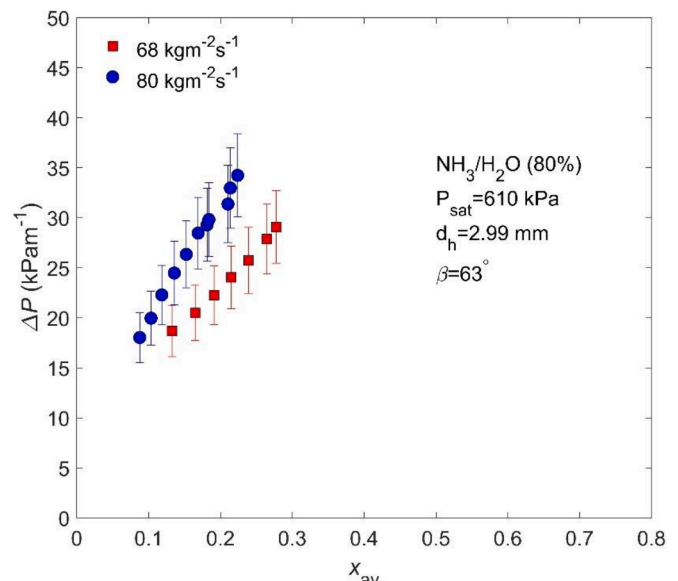
Fig. 20. Frictional pressure drop with varying averaged vapor quality at different mass fluxes. The bulk mass concentration is 80%.

4.3. Mass concentration of 88% and 80%

In Figs. 18-19, the NH_3/H_2O has a mass concentration of 88%, while Fig. 20 shows a bulk mass concentration of 80%. The frictional pressure drops are similar to those in Sections 4.1 and 4.2. Larger mass fluxes and higher averaged vapor qualities increase the frictional pressure drop.

The frictional pressure drops of NH_3/H_2O are slightly larger than those of pure NH_3 under similar mass fluxes and vapor qualities (Tao et al., 2020). The frictional pressure drops of NH_3/H_2O increase slightly with lower mass concentrations. This is the result of fluid properties instead of mass transfer resistance. According to the Appendix A, NH_3/H_2O has lower vapor density and larger liquid-vapor density ratio than NH_3. The density ratio of NH_3/H_2O increases with lower mass concentrations. The flow is separated flow. The two-phase pressure drop is mainly contributed by the vapor pressure drop. Larger density ratio increases vapor pressure drop. Moreover, the two-phase slip at the

interface is enhanced, and the momentum dissipation is aggravated.

5. Conclusions

In this paper, the condensation of high concentration NH_3/H_2O is experimentally investigated in a PHE. The mass concentrations are 80%, 88%, 91% and 96%. The results are compared with those of pure NH_3. The main conclusions are below:

- The flow patterns of high concentration NH_3/H_2O are considered to be the same as for NH_3. For full film flow, the phase change takes place at the two-phase interface. The apparent HTCs of NH_3/H_2O are slightly smaller than the HTCs of NH_3. In terms of partial film flow, the apparent HTCs of NH_3/H_2O are much smaller than the HTCs of NH_3. The process at the wetted zones is the same as full film flow. At the dry zones, the phase change takes place directly at the wall

surface. This characteristic lays the basis to develop the predictive model and will be analysed in the future work.

- The apparent HTCs increase noticeably with mass fluxes. The influence of vapor qualities depends on the mass concentrations and mass fluxes. When the mass concentration is 80%, the apparent HTCs stay almost constant or decrease with vapor qualities. For higher mass concentrations and large mass fluxes, the apparent HTCs increase with vapor qualities. The mass transfer resistance has significant influence at low mass concentrations and high vapor qualities.
- Frictional pressure drop increases significantly with vapor qualities and mass fluxes. When the vapor quality doubles, the frictional pressure drop becomes about twice larger. The increase rate with mass fluxes is more than that with vapor qualities. Larger liquid and vapor mass fluxes sharply aggravate the frictional pressure drop, showing the flow is separated. The frictional pressure drop of mixtures is affected by liquid-vapor density ratio, but mass transfer resistance has negligible effects. The NH_3 correlation of frictional

pressure drop can be extended to high concentration NH_3/H_2O with further verification (Tao and Infante Ferreira, 2020).

- Higher saturated pressure slightly decreases the apparent HTCs and frictional pressure drop. The saturated pressure plays a role by changing the vapor density and affecting the shear force.

Declaration of Competing Interest

The authors declare that they have no known competing financial interests or personal relationships that could have appeared to influence the work reported in this paper.

Acknowledgements

Appendix A

In Tables A1–A5, the thermodynamic properties of NH_3/H_2O are calculated using Refprop 10.0 (Lemmon et al., 2018), such as enthalpy, temperature and density. The transport properties of the mixture use Conde including thermal conductivity, dynamic viscosity and Prandtl number (Conde Engineering, 2006). All the fluid properties of pure NH_3 are calculated referring to Refprop 10.0 (Lemmon et al., 2018).

Table A1
Two-phase fluid properties of pure NH_3.

P_{sat} kPa	T_{sat} °C	ρ_G kg•m^{-3}	ρ_L kg•m^{-3}	μ_G μPa•s	μ_L μPa•s	Δh_{LG} kJ•kg^{-1}	σ mN•m^{-1}	λ_L W•$m^{-1}K^{-1}$	Pr_L –
600	9.3	4.75	626	9.36	149	1228	29.8	0.504	1.38
650	11.6	5.13	622	9.43	146	1219	29.1	0.499	1.37
700	13.8	5.51	619	9.50	142	1211	28.4	0.494	1.35
750	15.9	5.89	616	9.56	139	1203	27.7	0.490	1.34
800	17.9	6.27	614	9.63	137	1195	27.1	0.486	1.33
850	19.7	6.64	611	9.69	134	1187	26.5	0.482	1.32
900	21.5	7.02	608	9.74	132	1180	25.9	0.478	1.31

Table A2
Two-phase fluid properties of NH_3/H_2O with NH_3 mass concentrations of 96%.

P_{sat} kPa	T_{bubble} °C	T_{dew} °C	ρ_G kg•m^{-3}	ρ_L kg•m^{-3}	μ_G μPa•s	μ_L μPa•s	Δh_{LG} kJ•kg^{-1}	σ_{bubble} mN•m^{-1}	λ_L W•$m^{-1}K^{-1}$	Pr_L –
600	10.5	74.7	3.68	643	11.41	174	1468	37.3	0.530	1.56
650	12.9	76.7	3.98	639	11.49	170	1459	36.4	0.525	1.54
700	15.1	78.5	4.27	636	11.57	166	1451	35.6	0.520	1.52
750	17.2	80.3	4.57	633	11.64	163	1443	34.9	0.515	1.50
800	19.2	81.9	4.86	630	11.71	159	1436	34.2	0.511	1.49
850	21.1	83.5	5.15	628	11.78	156	1428	33.5	0.506	1.48
900	23.0	85.0	5.45	625	11.85	153	1421	32.9	0.502	1.46

Table A3
Two-phase fluid properties of NH_3/H_2O with NH_3 mass concentrations of 91%.

P_{sat} kPa	T_{bubble} °C	T_{dew} °C	ρ_G kg•m^{-3}	ρ_L kg•m^{-3}	μ_G μPa•s	μ_L μPa•s	Δh_{LG} kJ•kg^{-1}	σ_{bubble} mN•m^{-1}	λ_L W•$m^{-1}K^{-1}$	Pr_L –
600	12.3	90.2	3.53	664	11.76	209	1595	45.0	0.534	1.91
650	14.7	92.4	3.81	661	11.85	203	1587	44.1	0.530	1.87
700	17.0	94.4	4.09	658	11.93	198	1579	43.2	0.525	1.84
750	19.1	96.3	4.37	655	12.01	193	1571	42.4	0.521	1.81
800	21.1	98.1	4.65	652	12.09	189	1563	41.7	0.517	1.78
850	23.1	99.8	4.93	649	12.17	185	1556	40.9	0.513	1.76
900	24.9	101.4	5.21	647	12.25	181	1549	40.3	0.509	1.74

Table A4

Two-phase fluid properties of NH_3/H_2O with NH_3 mass concentrations of 88%.

P_{sat} kPa	T_{bubble} °C	T_{dew} °C	ρ_G kg•m^{-3}	ρ_L kg•m^{-3}	μ_G µPa•s	μ_L µPa•s	Δh_{LG} kJ•kg^{-1}	σ_{bubble} mN•m^{-1}	λ_L W•$m^{-1}K^{-1}$	Pr_L –
600	12.5	96.4	3.48	677	11.85	235	1663	48.7	0.535	2.16
650	15.9	98.7	3.75	673	11.94	228	1654	47.8	0.531	2.12
700	18.2	100.7	4.03	670	12.03	222	1646	46.9	0.526	2.07
750	20.4	102.7	4.30	667	12.11	216	1638	46.1	0.523	2.04
800	22.4	104.6	4.58	665	12.19	211	1630	45.3	0.519	2.00
850	24.4	106.3	4.85	662	12.27	206	1623	44.6	0.515	1.97
900	26.2	108.0	5.12	659	12.35	201	1616	43.9	0.512	1.94

Table A5

Two-phase fluid properties of NH_3/H_2O with NH_3 mass concentrations of 80%.

P_{sat} kPa	T_{bubble} °C	T_{dew} °C	ρ_G kg•m^{-3}	ρ_L kg•m^{-3}	μ_G µPa•s	μ_L µPa•s	Δh_{LG} kJ•kg^{-1}	σ_{bubble} mN•m^{-1}	λ_L W•$m^{-1}K^{-1}$	Pr_L –
600	17.4	108.5	3.38	709	11.98	318	1823	55.9	0.532	3.05
650	19.9	110.9	3.65	706	12.07	307	1814	54.9	0.528	2.96
700	22.2	113.2	3.92	703	12.15	297	1805	54.0	0.525	2.88
750	24.4	115.3	4.18	701	12.23	288	1797	53.2	0.522	2.80
800	26.5	117.2	4.45	698	12.31	280	1789	52.4	0.519	2.74
850	28.6	119.1	4.72	695	12.39	272	1781	51.7	0.517	2.68
900	30.5	120.9	4.98	693	12.46	265	1773	50.9	0.514	2.62

Appendix B

In Eqs. (B1)-(B16), the uncertainty propagation is explained referring to Taylor and Kuyatt (1994).

$$\dot{Q}_{test} = \dot{m}_w c_{p,w} \Delta T \tag{B1}$$

$$\delta\dot{Q}_{test} = \left|\delta\dot{m}_w \cdot c_{p,w}\Delta T\right| + \left|\dot{m}_w \cdot c_{p,w}\delta\Delta T\right| \tag{B2}$$

$$\frac{1}{U} = \frac{A \cdot \Delta T}{\dot{Q}_{test}} \tag{B3}$$

$$\delta\frac{1}{U} = \left|\frac{A}{\dot{Q}_{test}} \cdot \delta\Delta T\right| + \left|\frac{A\Delta T}{\dot{Q}_{test}^2}\delta\dot{Q}_{test}\right| \tag{B4}$$

$$\delta U = U^2 \cdot \delta\frac{1}{U} \tag{B5}$$

$$\frac{1}{\alpha_{aw}} = \frac{1}{U} - \frac{d_p}{\lambda_{wall}} - \frac{1}{\alpha_w} \tag{B6}$$

$$\delta\frac{1}{\alpha_{aw}} = \left|\delta\frac{1}{U}\right| + \left|\frac{1}{\lambda_{wall}}\delta d_p\right| + \left|\delta\frac{1}{\alpha_w}\right| \tag{B7}$$

$$\delta\alpha_{aw} = \alpha_{aw}^2 \cdot \delta\frac{1}{\alpha_{aw}} \tag{B8}$$

$$\Delta P_{fri,aw} = \Delta P_{exp,aw} - \Delta P_{inport,aw} - \Delta P_{outport,aw} - \Delta P_{mix,aw} + \Delta P_{de,aw} + \Delta P_{ele,aw} \tag{B9}$$

$$\delta\Delta P_{fri,aw} = \left|\delta\Delta P_{exp,aw}\right| + \left|v_L\frac{A_{tube}}{A_{port}}\left(1 - \frac{A_{tube}}{A_{port}}\right)\left(1 + \frac{v_G - v_L}{v_L}x\right)\cdot 2G_{tube}\delta G_{tube}\right| +$$
$$\left|v_L\left(\frac{1}{0.591} - 1\right)^2\left(1 + \frac{v_G - v_L}{v_L}x\right)G_{tube}\cdot\delta G_{tube}\right| + \left|2(v_G - v_L)(x_{in} - x_{out})G\cdot\delta G\right| \tag{B10}$$

$$G = \frac{\dot{m}_{aw}}{A_f} \tag{B11}$$

$$\delta G = \frac{1}{A_f}\delta\dot{m}_{aw} \tag{B12}$$

$$\dot{q} = \frac{\dot{Q}_{test}}{A} \tag{B13}$$

$$\delta\dot{q} = \frac{1}{A}\delta\dot{Q}_{test} \tag{B14}$$

$$\Delta h = \frac{\dot{Q}_{test}}{\dot{m}_{aw}} \tag{B15}$$

$$\delta\Delta h = \left| \frac{1}{\dot{m}_{aw}} \delta\dot{Q}_{test} \right| + \left| \frac{\dot{Q}_{test}}{\dot{m}_{aw}^2} \delta\dot{m}_{aw} \right| \tag{B16}$$

References

Atienza-Márquez, A., Bruno, J.C., Akisawa, A., Nakayama, M., Coronas, A., 2019. Fluids selection and performance analysis of a polygeneration plant with exergy recovery from LNG-regasification. Energy 176, 1020–1036.

Buscher, S., 2019. Visualization and modelling of flow pattern transitions in a cross-corrugated plate heat exchanger channel with uniform two-phase distribution. Int. J. Heat Mass Transf. 144, 118643.

Buscher, S., 2021. Two-phase pressure drop and void fraction in a cross-corrugated plate heat exchanger channel: impact of flow direction and gas-liquid distribution. Exp. Therm. Fluid Sci. 126, 110380.

Buscher, S., 2022. Digital image analysis of gas-liquid flow in a cross-corrugated plate heat exchanger channel: a feature-based approach on various two-phase flow patterns. Int. J. Multiph. Flow. 154, 104149.

Cerezo, J., Bourouis, M., Vallès, M., Coronas, A., Best, R., 2009. Experimental study of an ammonia–water bubble absorber using a plate heat exchanger for absorption refrigeration machines. Appl. Therm. Eng. 29, 1005–1011.

Chen, J., Zhu, K., Luo, X., Chen, Y., Yang, Z., 2019. Application of liquid-separation condensation to plate heat exchanger: comparative studies. Appl. Therm. Eng. 157, 113739.

Collier, J.G., Thome, J.R., 1994. Convective Boiling and Condensation. Clarendon Press, Oxford.

Conde Engineering, M., 2006. Thermophysical Properties of Ammonia-Water Mixtures For the Industrial Design of Absorption Refrigeration Equipment. Zurich.

Del Col, D., Azzolin, M., Bortolin, S., Zilio, C., 2015. Two-phase pressure drop and condensation heat transfer of R32/R1234ze (E) non-azeotropic mixtures inside a single microchannel. Sci. Technol. Built En. 21, 595–606.

Deng, H., Rossato, M., Fernandino, M., Del Col, D., 2019. A new simplified model for condensation heat transfer of zeotropic mixtures inside horizontal tubes. Appl. Therm. Eng. 153, 779–790.

DiPippo, R., 2004. Second Law assessment of binary plants generating power from low-temperature geothermal fluids. Geothermics 33, 565–586.

Fronk, B.M., Garimella, S., 2013. In-tube condensation of zeotropic fluid mixtures: a review. Int. J. Refrig. 36, 534–561.

Fronk, B.M., Garimella, S., 2016a. Condensation of ammonia and high-temperature-glide ammonia/water zeotropic mixtures in minichannels–Part I: measurements. Int. J. Heat Mass Transf. 101, 1343–1356.

Fronk, B.M., Garimella, S., 2016b. Condensation of ammonia and high-temperature-glide ammonia/water zeotropic mixtures in minichannels–Part II: heat transfer models. Int. J. Heat Mass Transf. 101, 1357–1373.

Ghim, G., Lee, J., 2016. Experimental evaluation of the in-tube condensation heat transfer of pure n-pentane/R245fa and their non-azeotropic mixture as an ORC working fluid. Appl. Therm. Eng. 106, 753–761.

Hart, J., Hamersma, P.J., Fortuin, J.M., 1989. Correlations predicting frictional pressure drop and liquid holdup during horizontal gas-liquid pipe flow with a small liquid holdup. Int. J. Multiph. Flow. 15, 947–964.

Heberle, F., Brüggemann, D., 2015. Thermo-economic evaluation of organic Rankine cycles for geothermal power generation using zeotropic mixtures. Energies 8, 2097–2124.

Hu, S., Ma, X., Zhou, W., 2017. Condensation heat transfer of ethanol-water vapor in a plate heat exchanger. Appl. Therm. Eng. 113, 1047–1055.

Huang, X., Zhang, J., Haglind, F., 2022. Experimental analysis of hydrofluoroolefin zeotropic mixture R1234ze (E)/R1233zd (E) condensation in a plate heat exchanger. Int. Commun. Heat Mass. 135, 106073.

Jankowski, T.A., Schmierer, E.N., Prenger, F.C., Ashworth, S.P., 2008. A series pressure drop representation for flow through orifice tubes. J. Fluids Eng. 130, 051204.

Jung, C.W., An, S.S., Kang, Y.T., 2014. Thermal performance estimation of ammonia-water plate bubble absorbers for compression/absorption hybrid heat pump application. Energy 75, 371–378.

Lemmon, E.W., Bell, I.H., Huber, M.L., McLinden, M.O., 2018. NIST Standard Reference Database 23: Reference Fluid Thermodynamic and Transport Properties-REFPROP, Version 10.0, National Institute of Standards and Technology. Standard Reference Data Program, Gaithersburg.

Liu, Q., Duan, Y., Yang, Z., 2014. Effect of condensation temperature glide on the performance of organic Rankine cycles with zeotropic mixture working fluids. Appl. Energ. 115, 394–404.

Liu, Q., Shen, A., Duan, Y., 2015. Parametric optimization and performance analyses of geothermal organic Rankine cycles using R600a/R601a mixtures as working fluids. Appl. Energ. 148, 410–420.

Luo, J., Lu, P., Chen, K., Luo, X., Chen, J., Liang, Y., Yang, Z., Chen, Y., 2023. Experimental and simulation investigation on the heat exchangers in an ORC under various heat source/sink conditions. Energy 264, 126189.

Macdonald, M., Garimella, S., 2016. Hydrocarbon mixture condensation inside horizontal smooth tubes. Int. J. Heat Mass Transf. 100, 139–149.

Mancin, S., Del Col, D., Rossetto, L., 2012. Condensation of superheated vapour of R410A and R407C inside plate heat exchangers: experimental results and simulation procedure. Int. J. Refrig. 35, 2003–2013.

Mazumder, S., Afroz, H.M.M., Hossain, M.A., Miyara, A., Talukdar, S., 2021. Study of in-tube condensation heat transfer of zeotropic R32/R1234ze (E) mixture refrigerants. Int. J. Heat Mass Transf. 169, 120859.

Mergner, H., Schaber, K., 2018. Performance analysis of an evaporation process of plate heat exchangers installed in a Kalina power plant. Energy 145, 105–115.

Shao, D.W., Granryd, E., 1998. Experimental and theoretical study on flow condensation with non-azeotropic refrigerant mixtures of R32/R134a. Int. J. Refrig. 21, 230–246.

Tao, X., Infante Ferreira, C.A., 2019. Heat transfer and frictional pressure drop during condensation in plate heat exchangers: assessment of correlations and a new method. Int. J. Heat Mass Transf. 135, 996–1012.

Tao, X., Dahlgren, E., Infante Ferreira, C.A., 2019. Condensation heat transfer and pressure drop of NH₃ and NH₃/H₂O within a plate heat exchanger. In: 25th IIR International Congress of Refrigeration. Montreal, Canada paper 727.

Tao, X., Dahlgren, E., Leichsenring, M., Infante Ferreira, C.A., 2020. NH₃ condensation in a plate heat exchanger: experimental investigation on flow patterns, heat transfer and frictional pressure drop. Int. J. Heat Mass Transf. 151, 119374.

Tao, X., Infante Ferreira, C.A., 2020. NH₃ condensation in a plate heat exchanger: flow pattern based models of heat transfer and frictional pressure drop. Int. J. Heat Mass Transf. 154, 119774.

Tao, X., Thanganadar, D., Patchigolla, K., 2022. Compact Ammonia/water absorption chiller of different cycle configurations: parametric analysis based on heat transfer performance. Energies 15, 6511.

Taylor, B.N., Kuyatt, C.E., 1994. Guidelines For Evaluating and Expressing the Uncertainty of NIST Measurement Results. National Institute of Standards and Technology, Gaithersburg, MD.

Thonon, B., Bontemps, A., 2002. Condensation of pure and mixture of hydrocarbons in a compact heat exchanger: experiments and modelling. Heat Transf. Eng. 23, 3–17.

Triché, D., Bonnot, S., Perier-Muzet, M., Boudéhenn, F., Demasles, H., Caney, N., 2017. Experimental and numerical study of a falling film absorber in an ammonia-water absorption chiller. Int. J. Heat Mass Transf. 111, 374–385.

Wang, J., Yan, Z., Zhou, E., Dai, Y., 2013. Parametric analysis and optimization of a Kalina cycle driven by solar energy. Appl. Therm. Eng. 50, 408–415.

Yu, J., Jiang, Y., Cai, W., Li, F., 2018. Heat transfer characteristics of hydrocarbon mixtures refrigerant during condensation in a helical tube. Int. J. Therm. Sci. 133, 196–205.

Yu, J., Jiang, Y., Cai, W., Li, X., Zhu, Z., 2019. Condensation flow patterns and heat transfer correction for zeotropic hydrocarbon mixtures in a helically coiled tube. Int. J. Heat Mass Transf. 143, 118500.

Zhang, X., He, M., Zhang, Y., 2012. A review of research on the Kalina cycle. Renew. Sust. Energ. Rev. 16, 5309–5318.

Zhang, Y., Jia, L., Dang, C., Ding, Y., Peng, Q., 2021a. Experimental investigation on flow condensation characteristics of binary mixture in a rectangular micro-channel. Int. Commun. Heat Mass. 123, 105195.

Zhang, J., Elmegaard, B., Haglind, F., 2021b. Condensation heat transfer and pressure drop characteristics of zeotropic mixtures of R134a/R245fa in plate heat exchangers. Int. J. Heat Mass Transf. 164, 120577.

Zhou, W., Hu, S., Ma, X., Zhou, F., 2018. Condensation heat transfer correlation for water-ethanol vapor mixture flowing through a plate heat exchanger. Heat Mass Transf. 54, 1–9.

Zhuang, X.R., Chen, G.F., Guo, H., Song, Q.L., Tang, Q.X., Yang, Z.Q., Zou, X., Gong, M.Q., 2018. Experimental investigation on flow condensation of zeotropic mixtures of methane/ethane in a horizontal smooth tube. Int. J. Refrig. 85, 120–134.